Tunable Three-Dimensional Architecture of Nematic Disclination Lines

Alvin Modin[a], **Biswarup Ash**[b], **Kelsey Ishimoto**[a], **Robert L. Leheny**[a], **Francesca Serra**[a, c], **and Hillel Aharoni**[b]

[a]Department of Physics and Astronomy, Johns Hopkins University, Baltimore, MD 21218, USA; [b]Department of Physics of Complex Systems, Weizmann Institute of Science, Rehovot 76100, Israel; [c]Department of Physics, Chemistry, and Pharmacy, University of Southern Denmark, Odense, DK-5230 Denmark

This manuscript was compiled on July 22, 2024

Disclinations lines play a key role in many physical processes, from the fracture of materials to the formation of the early universe. Achieving versatile control over disclinations is key to developing novel electro-optical devices, programmable origami, directed colloidal assembly, and controlling active matter. Here, we introduce a theoretical framework to tailor three-dimensional disclination architecture in nematic liquid crystals experimentally. We produce quantitative predictions for the connectivity and shape of disclination lines found in nematics confined between two thinly spaced glass substrates with strong patterned planar anchoring. By drawing an analogy between nematic liquid crystals and magnetostatics, we find that: i) disclination lines connect defects with the same topological charge on opposite surfaces and ii) disclination lines are attracted to regions of the highest twist. Using polarized light to pattern the in-plane alignment of liquid crystal molecules, we test these predictions experimentally and identify critical parameters that tune the disclination lines' curvature. We verify our predictions with computer simulations and find non-dimensional parameters enabling us to match experiments and simulations at different length scales. Our work provides a powerful method to understand and practically control defect lines in nematic liquid crystals.

Liquid crystals | Topological defects | Soft Matter physics | ...

Topological singularities link physically distinct phenomena – they mediate phase transitions (1), act as organizational centers in biological systems (2), and steer the trajectory of light (3, 4). Various topological defect configurations are present in nematic liquid crystals (LCs), fluid-like materials with long-range orientational molecular order. Disclination lines arise when nematic LCs are frustrated by incompatible boundary conditions. These one-dimensional singularities can be facilely formed and visualized, making nematic LCs an ideal test bed for studying defect structures and interactions. Manipulating disclination lines in LCs also has practical applications in directed self-assembly (5, 6), tunable photonics (7), and re-configurable microfluidic devices (8, 9). To effectively utilize the potential of disclinations for these applications, it is essential to develop a set of fundamental rules that govern their formation and connectivity.

Recent advances in spatial patterning of liquid crystal alignment have enabled greater control over the structure of disclination lines. For example, imprinted nano-ridges on glass substrates have been used to precisely shape defect lines, revealing insights into their energy, structure, and multi-stability (10, 11), and the corners of faceted colloids have been shown to act as prescribed sites for nucleating defect lines to connect the particles(12).. Using light to impose LC alignment at photosensitive substrates is an equally powerful tool. Photoalignment has enabled the design of free-standing disclination loops(13–15) and periodic disclination arrays with different morphologies and properties (16–21).

In this work, we introduce a general framework for creating arbitrarily shaped three-dimensional (3D) disclination line architecture in nematic liquid crystals. Our framework provides both an approach to understanding otherwise unintuitive defect line behavior and a new strategy for designing disclination lines for potential applications. As an example, we show a structure where the projection of disclination lines on a two-dimensional (2D) plane forms the shape of a heart (Fig. 1). In the experiment, light-sensitive layers on parallel glass substrates align the nematic at the surfaces in patterns decorated with pairs of 2D surface defect nucleation sites (Fig.1*A*). The 2D defects are characterized by winding numbers - the degree of rotation of the nematic director around the defect divided by 2π - of $+1/2$ and $-1/2$. Aligning opposite-charged defects on opposing substrates, we observe that the confined LC forms a pair of disclination lines that primarily run through the mid-plane of the cell to connect surface defects on the same substrate (Fig. 1*B*). This configuration is a stable, equilibrium state, confirmed by numerical simulations (Fig.1*C*-*D*).

To understand the paths that the disclination lines take, we draw an analogy between the elastic distortion of a nematic and the magnetostatic field of current-carrying wires. Using

Significance Statement

Topological defects are universal patterns of nature. Nematic liquid crystals are ideal test beds for studying defects, particularly one-dimensional, linear disclinations. Understanding disclination structures and interactions is critical to developing novel optical devices, meta-materials and for directing self-assembly at the micro and nanoscale. Recent work in manipulating defects in liquid crystals has focused on creating non-trivial morphologies and periodic arrays. Here, we introduce a set of design principles that enables quantitative predictions for the connectivity and shape of disclination lines under general assumptions. Using experiments and numerical simulations, we show that this framework can create arbitrarily shaped three-dimensional disclination architecture whose structure can be tuned *in situ*. Our system provides both physical insight and powerful tools to induce desired shape changes of defect lines, opening opportunities to design new types of smart materials.

A.M built the experimental system and performed the experiments and data analysis. B.A. performed the simulations. K.I. contributed to building the experimental system. R.L. and F.S. supervised the experimental work. H.A. supervised the theoretical work. H.A. and F.S. designed the project. All authors wrote the paper.

The authors do not have competing interests.

[1] A.M. and B.A. contributed equally to this work.

[2] To whom correspondence should be addressed. E-mail: hillel.aharoni@weizmann.ac.il or serra@sdu.dk

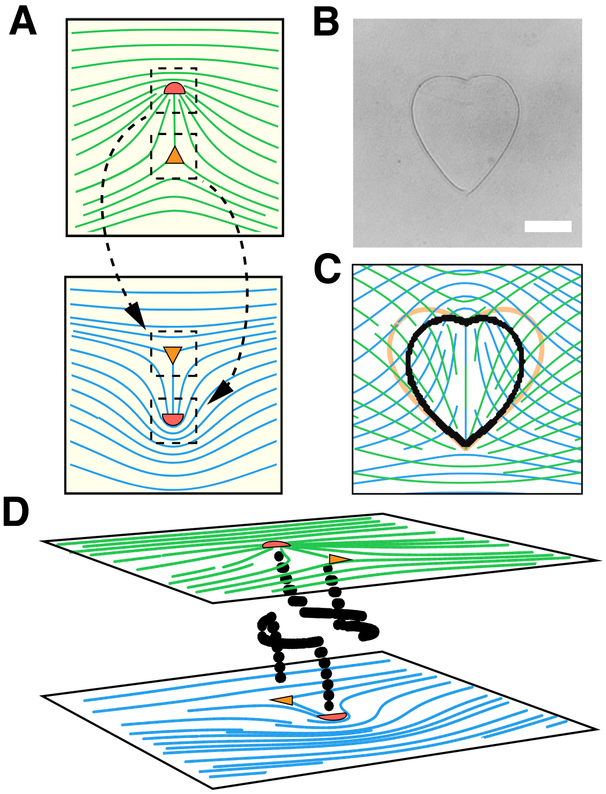

Fig. 1. Designing three-dimensional disclination line architecture. (*A*) Schematics of the two-dimensional surface patterns imprinted onto substrates coated with a photo-sensitive layer (Brilliant Yellow). Topological defects with charge $+1/2$ (red semi-circle) and $-1/2$ (orange triangle) act as nucleation sites for disclination lines. The substrates are aligned so that defects of opposing strength are in registry with each other. (*B*) Disclination lines viewed under bright-field microscopy form a heart-shaped structure (scale bar: 25 μm). This configuration corresponds to a stable equilibrium state. Top view (*C*) and side view (*D*) of the disclination structure obtained from simulation using the patterns in (*A*) as surface boundary conditions. The observed two-dimensional projection (black points) is a balance between the attraction of defect lines to locations where the top and bottom surface patterns are perpendicular (orange lines in (*C*)) and their line tension. (*D*) A side view of the defect configuration obtained in the simulation reveals that the disclination lines primarily run through the mid-plane of the cell and connect surface defects of opposite charge on the same substrate.

this analogy, we experimentally and numerically verify two key rules: (i) disclination lines either connect surface defects on opposing substrates with the same winding number or surface defects on the same substrate having opposite winding numbers; (ii) the lines' paths depend on the interplay between forces driving them to regions of maximum twist set by the confining pattern and the disclination line tension. We utilize these two design principles to create the heart-shaped disclinations shown in Fig. 1. Our proposed framework enables the design of tunable 3D liquid crystal-based disclination networks for applications in re-configurable optics, photonic devices, and responsive matter.

The following sections explain the magnetostatic analogy and its outcomes. Subsequently, we test specific predictions with experiments and simulations. Finally, we revisit the structure in Fig. 1 to explain how we designed the heart-shaped lines and how disclination shapes can be tailored by varying temperature.

Results and Discussion

Magnetostatics model. Distortions of the nematic director field are described by the Frank-Oseen elastic free energy (22),

$$F_{\mathrm{el}} = \int \Big[\frac{K_1}{2} \left(\nabla \cdot \hat{\mathbf{n}}\right)^2 + \frac{K_2}{2} \left(\hat{\mathbf{n}} \cdot \nabla \times \hat{\mathbf{n}}\right)^2 + \frac{K_3}{2} \left(\hat{\mathbf{n}} \times \nabla \times \hat{\mathbf{n}}\right)^2 \Big] \, dV, \qquad [1]$$

with $\hat{\mathbf{n}}$ the nematic director and $K_{1,2,3}$ the splay, twist, and bend elastic constants, respectively. We consider a nematic placed between two parallel plates with (sufficiently strong) patterned planar anchoring on them, separated by a spacing t much smaller than their lateral dimensions. Under these conditions, we make the following key assumption: in equilibrium, the nematic director is planar everywhere within the cell, not only at the boundaries. This is analogous to the Kirchhoff-Love assumptions in plate elasticity theory (23). The nematic director field then takes the form $\hat{\mathbf{n}} = (\cos\theta, \sin\theta, 0)$, where $\theta(x, y, z)$ is the director's azimuthal angle in the xy-plane. In addition, we use the two-constant approximation, with $K_1 = K_3 \equiv K$, which is valid near the nematic-isotropic transition for low molecular weight thermotropic nematic LCs, particularly 4'-octyl-4-biphenylcarbonitrile (8CB) (24) used in our experiments. Eq. 1 then assumes the simple form,

$$F_{el} = \int \left[\frac{K}{2} \left[(\partial_x \theta)^2 + (\partial_y \theta)^2 \right] + \frac{K_2}{2} (\partial_z \theta)^2 \right] dV. \qquad [2]$$

Further simplification is obtained by rescaling the z-axis using $\tilde{z} = z\sqrt{K/K_2}$ (defined on a domain of thickness $\tilde{t} = t\sqrt{K/K_2}$), and redefining $\nabla \equiv (\partial_x, \partial_y, \partial_{\tilde{z}})$, so that

$$F_{el} = \frac{K}{2} \int |\nabla\theta|^2 \, d\tilde{V}. \qquad [3]$$

The functional in Eq. 3 implies that, in equilibrium, $\theta(x, y, \tilde{z})$ is a harmonic function. However, this property breaks down along disclination lines; at the defect core, the nematic order vanishes, and θ is not defined. Around the defect line, Eq. 3 admits a nontrivial quantized integral,

$$\oint d\ell \cdot \nabla\theta = 2\pi q, \qquad q \in \mathbb{Z}/2. \qquad [4]$$

Together Eq. 3 and 4 establish an exact mathematical analogy of the nematic cell to magnetostatics, as previously identified by de Gennes (22). In the analogy, the planar director's azimuthal angle θ plays the role of a magnetic scalar potential, whose gradient is the magnetic field (it is a polar vector, whose polarity stems from the gradient operator and not from the apolar nematic director). Disclination lines are current-carrying wires. Their existence renders θ ambiguous; however, the half-integer quantization of the current exactly corresponds to the nematic $\theta \cong \theta + \pi\mathbb{Z}$ congruence.

The disclination wires are flexible and stretchy. Each wire is associated with a line tension γ, the outcome of melting of the nematic order at the defect core to alleviate the diverging elastic energy. Approximately, γ is proportional to Kq^2; however, there are logarithmic corrections as well as bending and torsion costs that depend on the line and cell geometry (22, 25, 26). These corrections become significant near the nematic-isotropic phase transition as the defect core size diverges. For simplicity, we ignore these corrections and treat γ as a constant. Similarly to other material parameters, namely K, K_2, γ may depend on temperature in a non-trivial way.

Forces on wires. To study the shape of disclination wires, we calculate the effective forces acting on them (see *SI Appendix* for full derivations). There are three forces (per unit length) acting on the wires:

1. The strong anchoring on the two surfaces acts as magnetic mirrors. Disclination wires are repelled by these mirrors (alternatively, by the mirror image wires) and pushed toward the mid-plane between the two boundary surfaces by a force
$$\mathbf{f}_M = -\frac{\pi^2 K q^2}{\tilde{t}} \tan\left(\frac{\pi \tilde{z}}{\tilde{t}}\right)\hat{\mathbf{z}}. \tag{5}$$
2. The anchoring planar angles, $\theta_{t,b}(x, y)$ on the top/bottom surfaces, respectively, are analogous to an external magnetic field that exerts a Lorentz-like force on disclination wires:
$$\mathbf{f}_B = \frac{2\pi K q}{\tilde{t}} \left(\theta_t - \theta_b - q\pi\right) \hat{\mathbf{T}} \times \hat{\mathbf{z}}, \tag{6}$$
where $\hat{\mathbf{T}}$ is the unit tangent to the defect line. This force pulls defect lines horizontally towards regions where the top and bottom are at a $\Delta\theta \equiv \theta_t - \theta_b = q\pi$ angle difference from each other.
3. The line tension of the wires exerts a force
$$\mathbf{f}_\gamma = \gamma\kappa\hat{\mathbf{N}}, \tag{7}$$
where κ is the curvature of the wire and $\hat{\mathbf{N}}$ its normal in the Frenet-Serret frame.

The equilibrium shape of a disclination line is obtained by the balance of $\mathbf{f}_M$, $\mathbf{f}_B$, and $\mathbf{f}_\gamma$.

This force balance can characterize the geometry of defect lines connecting to surface defects. A disclination line emerges perpendicularly from a surface topological defect due to the magnetic repulsion described by Eq. 5. For a surface defect $|q| > \frac{1}{2}$ we expect a split into $2|q|$ "atomic" lines of magnitude $\frac{1}{2}$ arising from the mutual repulsion between them (as was observed in (10, 17)). By the balance of forces, $\mathbf{f}_M$ and $\mathbf{f}_\gamma$ lines emerging from defects turn horizontally into the mid-plane over a typical length scale $\sim \frac{\gamma}{K}\tilde{t} \equiv \frac{\gamma}{\sqrt{KK_2}}t$. Thus, defect lines whose lateral span is much larger than this scale traverse within the mid-plane for the more significant part of their trajectories.

Connectivity of surface defects. We study the topological rules of connecting – with disclination wires – surface defects patterned on two confining surfaces. Each surface defect is characterized by a winding number q, defined by a closed loop Γ around the defect core as $\frac{1}{2\pi}\oint_\Gamma \nabla\theta \cdot d\ell$. By current conservation, a disclination line can connect two surface defects of the *same q on opposite surfaces*; or two surface defects of *opposite q on the same surface*. Alternatively, disclinations can escape to the sides of the system or form a closed loop. Planarity of the director field forbids connection between a top-surface $+1/2$ defect with a bottom-surface $-1/2$, even though this would be topologically allowed in a 3D nematic liquid crystal (27).

Experimental Tests.

Test of Design Principles. To verify these connectivity principles experimentally, we create a LC cell where the bottom and top surfaces contain a single, isolated $q = -1/2$ or $+1/2$ defect, respectively (Fig. 2 *A-C*), utilizing the custom built photo-alignment system described in *Materials and Methods* and *SI Appendix, Fig. S1* (28–30). We shine linearly polarized light on glass coated with a light-sensitive alignment layer (Brilliant Yellow). The alignment layer molecules give planar alignment to the LC, with a direction that is perpendicular to the polarization of the incident light. By spatially patterning the light polarization, we imprint half-integer defect nucleation sites onto confining glass substrates. The defects on each surface are photo-patterned within a circular patch of diameter $d \approx 75\mu$m. Under crossed-polarizers, the dichroic properties of the Brilliant Yellow dye enable us to view the patterned regions on the confining glass substrates before filling them with LC. We align the circular patches on each substrate to overlap, ensuring that defect cores of opposing topological charges are in registry. Once substrates are secured with epoxy resin, we carefully measure the cell thickness and inject pre-heated 8CB LC into the cell, allowing it to slowly cool until it reaches the nematic phase at $\sim 36°$C.

The resulting defect structure follows the connectivity rules: rather than a single disclination line connecting the surface defects as might be expected (27), two disclination lines emerge from the defect cores and escape to the sides along the mid-plane, as can be seen from a side view of the numerical simulation in Fig. 2*A* and from the top view in experiments (Fig. 2*B*) and simulations (Fig. 2*C*). Indeed, this connectivity rule gives rise to the two extended lines that make the heart shape in Fig. 1 rather than two defect lines connecting surface defects directly facing each other. For verification, we run the same experiment and simulation with $+1/2$ surface defects patterned onto confining substrates (see *SI Appendix, Fig. 2*). A vertical disclination line connects the top and the bottom surface defects, as is permitted in this case by current conservation.

The effect of varying the patterned boundary conditions can be seen in Fig. 2(*D-F*). Here, we preserve the topological charge of each surface pattern but introduce a homogeneously aligned region that alters the geometric structure of the $\pm 1/2$ defects. The new surface pattern modifies the areas where $\Delta\theta\,(x, y)$ are orthogonal. The new regions where $\mathbf{f}_B = 0$ lead to a reduced angular separation of the two defect lines from π (Fig. 2*B-C*) to $\pi/2$ (Fig. 2*E-F*). For both designs, the disclination wires do not bend and $\kappa \approx 0$, implying that $\mathbf{f}_\gamma$ has little to no effect on the positioning of the lines.

Tuning the curvature of disclination architecture. When the imposed surface patterns result in curved disclination lines, the line tension $\mathbf{f}_\gamma$ becomes important. $\mathbf{f}_\gamma$ opposes $\mathbf{f}_B$, acting to minimize the wire's curvature. The competition between these two forces causes the trajectory of the two disclination lines in Fig. 1*D* to deviate from regions where $\Delta\theta\,(x, y) = \pi/2$. The shape of the disclination lines can then be tuned by changing the magnitude of $\mathbf{f}_B$ and $\mathbf{f}_\gamma$, which vary differently with temperature due to the temperature-sensitive behavior of γ and the elastic constants K, K_2. As described below, by tuning the disclination shape, we measure $\gamma/\sqrt{KK_2}$ at various temperatures, enabling us to map our experimental observations to simulations.

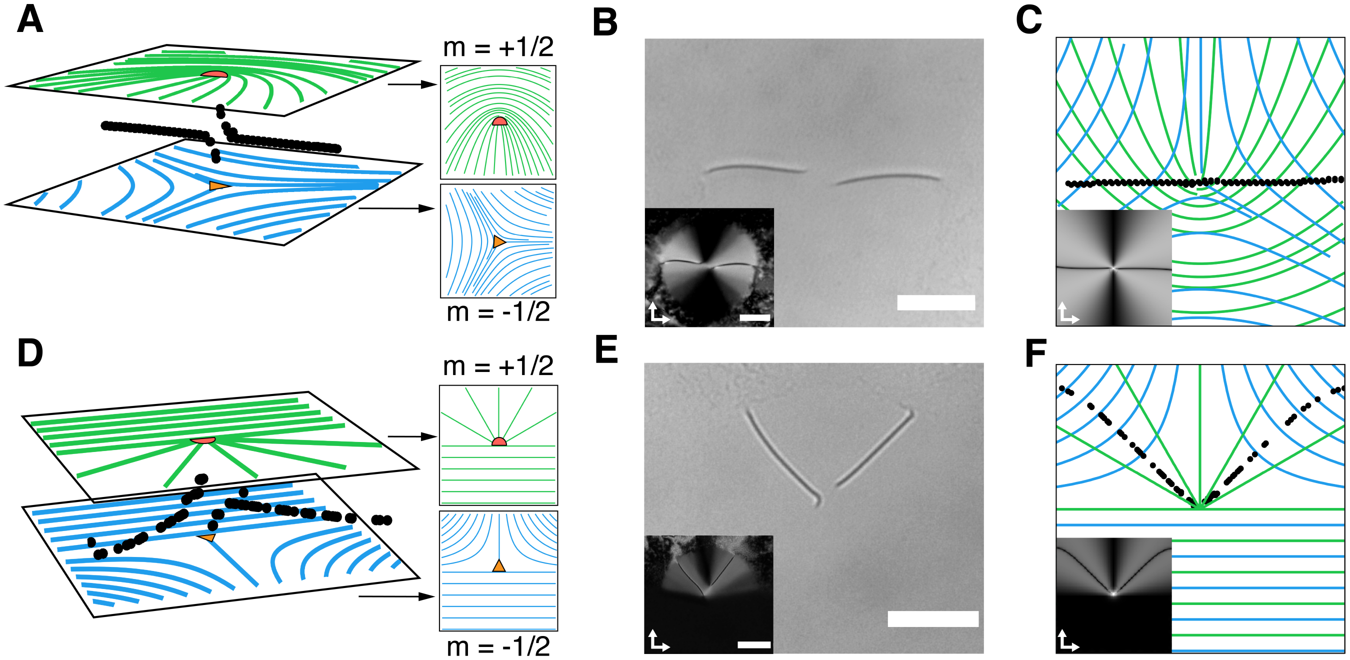

Fig. 2. Surface defect connectivity. (*A*) When two canonical surface defects with $\pm 1/2$ charge are imposed as boundary conditions, the planarity of the director field forbids the connection of the top and bottom surface defects with a single defect line. The equilibrium state obtained from numerical minimization of Landau de Gennes energy corresponds to two disclination lines (black points) nucleating at the surface defect cores and extending towards the boundaries.(*B*) Bright-field microscopy images where two confining surfaces are photo-aligned with isolated $\pm 1/2$ surface defects corresponding to the pattern used in (*A*) . Inset: polarized light microscopy image.(*C*) Two-dimensional projection of the numerical results in (*A*). Inset: The expected polarized optical microscopy (POM) texture reconstructed from the director field using Jones calculus. (*D*) Preserving the topological charge of the surface defects while altering their geometric structure changes the regions where $\Delta\theta = \pi/2$. The equilibrium state for these boundary conditions corresponds to two disclination lines now at a relative angle of $\pi/2$. (*E*) Bright-field microscopy images where two confining surfaces are photo-aligned with isolated $\pm 1/2$ surface defects corresponding to the pattern used in (*D*). (*F*) Two-dimensional projections of the numerical results in (*D*). Inset: The expected POM texture reconstructed from the director field using Jones calculus. Scale bars: 25μm.

To illustrate the tuning of disclination shape, we construct LC cells whose confining surfaces are each photo-patterned with a single $+1/2$ defect. The substrates are rotated so that the defects are oriented with respect to one another by an angle θ_0 and are translated so that a horizontal distance ℓ separates the defect cores (Fig. 3*A, B*). In this design, the 2D projection of the patterns contains a locus of points where $\Delta\theta = \pi/2$ forms a circular arc segment with an opening angle $2\theta_0$ connecting the defects. Once a cell is filled with 8CB, a disclination line forms to connect the two defect cores (Fig. 3*C*).. In general, the line does not follow the arc with opening angle θ_0 due to $\mathbf{f}_\gamma$. However, along any circular disclination arc that passes between the two surface defect cores, both Eq. 6 and 7 are uniform. Thus, in equilibrium, the disclination still forms an arc, and finding its curvature through force balancing is a simple algebraic problem:

$$0 = (\mathbf{f}_B + \mathbf{f}_\gamma) \cdot \hat{\mathbf{N}} = \frac{\pi K}{\tilde{t}}\left(\frac{\alpha}{2} - \theta_0\right) + \gamma \frac{2}{\ell} \sin\frac{\alpha}{2}, \qquad [8]$$

where α is the opening angle of the arc. Rewriting Eq. 8 in a dimensionless form, we obtain the following transcendental equation:

$$\frac{\alpha}{2} + \tilde{\gamma} \sin\frac{\alpha}{2} = \theta_0, \qquad [9]$$

where $\tilde{\gamma} = \frac{2}{\pi}\frac{\gamma}{\sqrt{KK_2}}\frac{t}{\ell}$. As expected, in the limit of vanishing line tension, α tends to $2\theta_0$, where f_B vanishes. In the limit of infinite line tension, α tends to zero so that f_γ vanishes. Line tension's relative importance in determining the defect line's contour is described by the dimensionless parameter $\tilde{\gamma}$.

Equation 9 captures the effect of line tension in reducing the curvature of an arced disclination line. Rearranging it again, we find that,

$$\frac{\gamma}{\sqrt{KK_2}} = \frac{\pi}{2\kappa t}\left[\theta_0 - \arcsin\left(\frac{\ell\kappa}{2}\right)\right]. \qquad [10]$$

The equation above links the material parameter $\gamma/\sqrt{KK_2}$ to the deviation of the disclination arc's curvature κ from its zero-line tension limit. Thus, the temperature dependence of $\gamma/\sqrt{KK_2}$ can be measured directly in 8CB from the temperature dependence of the line curvature. We track the variation of $\alpha = 2\arcsin(\ell\kappa/2)$ as a function of temperature across θ_0 ranging from 30° to 105° (see *Materials and Methods* for details of the image analysis). When a disclination line is formed by an initial $\theta_0 = 105°$, the curvature deep in the nematic phase ($T = 35°$C) is small (Fig. 3*C*). Increasing the temperature towards the nematic-isotropic transition, we observe an increase in κ (and hence α) since $\mathbf{f}_\gamma$ decreases more rapidly than $\mathbf{f}_B$ on heating (Fig. 3*D*). Equation 10 is confirmed by the collapse in Fig. 3*E* of measurements held at different values of t, ℓ and θ_0 onto the same curve that only depends on material properties of the LC. This affirms the validity of approximating γ with a constant.

Fig. 3*E* shows the monotonic temperature dependence of $\gamma/\sqrt{KK_2}$ in a nematic 8CB, ranging approximately between 12 and 18. We follow the protocol of Fig. 3 to also estimate $\gamma/\sqrt{KK_2}$ in our numerical simulations (see *SI Appendix* for details); we analyze arced defect configurations for different

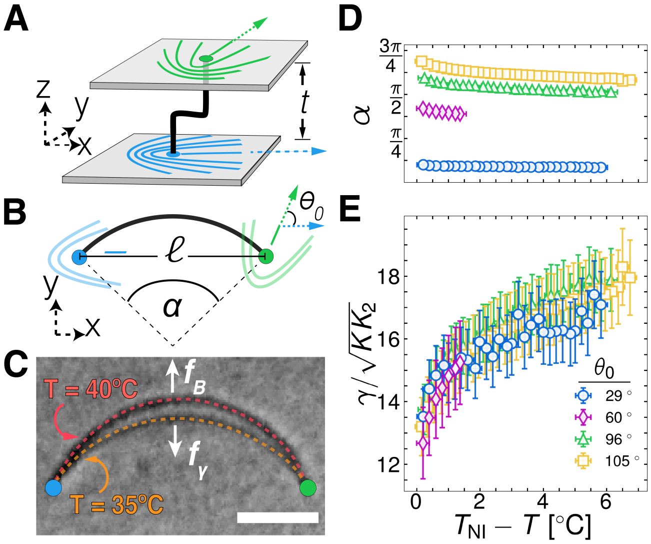

Fig. 3. Measuring the line tension of a disclination. (*A*) Diagrams of the geometry used to create arced disclination lines. Initially, $+1/2$ surface defects are imposed as anchoring conditions in a nematic cell. The substrates are then rotated and displaced with respect to one another. (*B*) When viewed from the top, the defects cores are separated by a distance ℓ and their lines of symmetry form an angle θ_0. The two-dimensional projection of the resulting disclination line is a portion of a circular arc with a central angle α. (*C*) Bright-field microscopy overlapped images of disclination lines at two different temperatures. The disclination line's curvature depends on the balance of two opposing forces f_γ and f_B, whose magnitudes depend on temperature (scale bar: 10μm, dashed lines are guides for the eye). (*D*) Varying the temperature of the nematic, therefore, results in a change in the defect line curvature and in the angle α as shown in the curves obtained for different values of θ_0. (*E*) When the measured values of t, ℓ, and θ_0 are all accounted for, the implied values of $\gamma/\sqrt{KK_2}$ all collapse onto the same curve as a function of temperature.

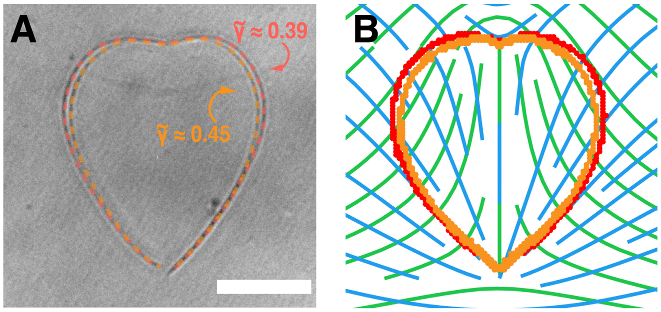

Fig. 4. Tunable disclination line architecture (*A*) Bright-field microscopy image of heart-shaped disclination lines measured for two different temperatures, corresponding to different values of $\tilde{\gamma}$ (scale bar: 25 μm, dashed lines are guides for the eye). (*B*) Defect configurations obtained in the simulation for two different sets of parameters l, t, chosen such that the values of $\tilde{\gamma}$ are the same in simulation and experiment. The change in the structure of the disclination architecture in both experiment and simulation is captured by $\tilde{\gamma}$.

values of t, ℓ and θ_0, and extract α from which we obtain a mean $\gamma/\sqrt{KK_2} = 3.3 \pm 0.1$. This value is not within the experimental range. However, for every experiment, we can now match a simulation held at the same value of $\tilde{\gamma} = \frac{2}{\pi}\frac{\gamma}{\sqrt{KK_2}}\frac{t}{\ell}$, by compensating for the different values of $\frac{\gamma}{\sqrt{KK_2}}$ with inversely different values of the aspect ratio $\frac{t}{\ell}$. In simulations, we tweak $\tilde{\gamma}$ not with temperature but with aspect ratio.

We now revisit Fig. 1 and the heart-shaped disclination lines. These are generated using patterns described in detail in the *Materials and Methods.*

We control the cusps of the heart by the directions of maximum twist around the defects as in Fig. 2. When 8CB is cooled by ≈ 6°C from the nematic-isotropic transition, the increase in $\tilde{\gamma}$ constricts the lobes of the heart-shaped disclination lines (Fig. 4*A*). We know the value of $\tilde{\gamma}$ at each temperature from the thickness of the cell, the lateral separation between the two surface defects, and Fig. 3E. Simulations with the same values of $\tilde{\gamma}$, obtained by changing the values of t and ℓ, qualitatively capture a similar change in the structure of the disclination architecture Fig. 4*B*. It is remarkable that despite the experimental uncertainty and the use of different system sizes in the experiment and simulation, the resulting defect configurations for the same values of $\tilde{\gamma}$ are in good agreement.

Conclusion

This work introduces a novel framework for creating and tuning 3D disclination lines in a nematic liquid crystal. When disclination lines are nucleated by surface defects, their connectivity and trajectories are analogous to current-carrying wires near a current-free surface. Whether or not surface defects may connect to each other can be explained by treating the topologically charged disclination lines as wires that must conserve current. Similarly, substrates imprinted with surface-anchoring conditions exert a Lorentz-like force on the wires, pushing them towards regions where the anchoring conditions on opposing substrates are orthogonal. When the patterns promote wires to curve, they experience an additional force from line tension that decreases the curvature. This force can be tuned in both experiments and simulations by changing a dimensionless parameter, $\tilde{\gamma}$.

We verified these connectivity principles through a series of experiments. By appropriately designing surface anchoring conditions, we created a three-dimensional structure whose two-dimensional projection resembles a heart. We tuned its shape by varying the temperature and recreated the results using numerical simulations.

The magnetostatic analogy strongly relies on the nematic director being planar. In our system, the anchoring strength from Brilliant Yellow on the confining parallel plates is sufficient to achieve bulk planarity, but alternative methods may be used in other cases. One such method is to use a negative dielectric anisotropy liquid crystal (such as CCN-47). Application of an AC field would then force the director to lie in the plane perpendicular to the field(31). If needed, surface patterning may be used to break the in-plane degeneracy at the boundaries. This technique may be implemented to apply the magnetic analogy to system geometries other than the space between adjacent parallel plates.

Our design principles can be used to interpret similar results observed in recent experiments with disclination lines created by patterned surfaces (14–16, 18, 32, 33). These principles can further be used to construct more complex disclination architecture, advancing the design of tunable 3D liquid crystal-based disclination networks for applications of molecular self-assembly, re-configurable optics, photonic devices, and responsive matter. Furthermore, we have shown that the equilibrium shape of disclination lines depends on temperature and aspect ratio, opening the door for multi-state systems, switchable by varying the temperature or thickness of the cell.

Materials and Methods

Substrate preparation. Photosensitive material Brilliant Yellow (BY, Sigma-Aldrich) was mixed with n,n-dimethylformamide (DMF) solvent at 1 wt.% concentration. Glass substrates (Fisher Scientific) were washed in an ultrasonic bath with Hellmanex liquid detergent (Fisherbrand), followed by successive washes in acetone, ethanol, and isopropyl alcohol, and then dried with N_2 gas. The BY-DMF solution was spin-coated on the substrates at 3000 RPM for 45 seconds. After spin-coating, the substrates were baked at 95°C for 15 minutes. Spin-coating and baking processes were conducted at a relative humidity of 35% or lower(34).

Surface patterns used in experiments and simulations. In the experiment and simulations, we impose a patterned planar director field, where the nematic director field takes the form $\hat{\mathbf{n}} = (\cos\theta, \sin\theta, 0)$ at the top and bottom surfaces. In Figs. 1 and 4 ,the surface pattern at the top surface is represented by

$$\theta_{\mathrm{t}}(x,y) = \frac{1}{2}\left(\tan^{-1}\frac{y-1}{x} - \tan^{-1}\frac{y+1}{x} + \frac{x}{\sqrt{x^2+(y+1)^2}} - \frac{x}{\sqrt{x^2+(y-1)^2}}\right), \qquad [11]$$

while $\theta_{\mathrm{b}}(x,y) = -\theta_{\mathrm{t}}(x,y)$. For the $\pm 1/2$ surface defect patterns used in Figs. 2,3 we have

$$\theta(x,y) = \pm\frac{1}{2}\tan^{-1}\left(\frac{y}{x}\right) \qquad [12]$$

.

Patterned surface alignment. Surface patterns generated according to Eqs. 11 and 12 were imprinted as boundary conditions on substrates using a custom-built photo-patterning setup consisting of a polarized LED source (30) feeding into the side port of a bright-field inverted microscope body (TI Eclipse TE2000).

Segmented images were designed in Keynote and generated using a LED-based projector (Sony MPL-C1A) connected to a peripheral optical path (*SI Appendix* Fig. S1*A*). The projector operates using three time-modulated laser diodes. To match the absorption band of the BY-DMF solution, we use the blue ($\lambda = 445$nm) diode. Images generated by the projector first pass through two aspheric condenser lenses (Thorlabs, ACL50832U) with focal lengths $f = 32$ mm, separated by 64 mm. These lenses collimate the illumination. Two achromatic doublet lenses ($f = 100$ mm, Thorlabs, AC508-100-A-ML and $f = 200$ mm, Thorlabs, AC508-200-A-ML) bring the image into focus at the infinity-corrected plane near the microscope's side port. Before entering the microscope body, the image passes through a linear polarizer.

Once inside the body, the image is reflected by a dichroic mirror, picked up by an infinity-corrected tube lens, and collected by a microscope objective (20x, Nikon S Plan Fluor ELWD) that focuses the light onto a BY-coated substrate. Upon irradiation with linearly polarized light, the photosensitive azo-dye molecules orient perpendicularly to the plane of polarization, setting the preferred alignment direction of the nematic director $\hat{\mathbf{n}}$. Designed patterns following Eq. 11 were discretized into level sets where the director orientation (and the polarization direction of the incident light) varied by $\pi/16$ (see *SI Appendix* Fig. S1*B*). Patterns generated according to Eq. 12 were discretized into pie slices with opening angle $\pi/16$ such that the cores of the surface defects were located at the vertex of each slice.

Sample preparation. After photo alignment, patterned regions on substrates were aligned and fixed using epoxy glue (Loctite) to create a liquid crystal cell. After cell assembly, we use spectroscopic reflectometry to measure the cells' thickness t, obtained from the absolute reflectance spectra (Oceanview) fit using custom Matlab code. Cells are subsequently filled with 4'-n-octyl-4-cyano-biphenyl (8CB, Nematel GmbH) liquid crystal, pre-heated into the isotropic phase by capillary flow. After cells are filled, they are sealed on their ends using UV curable resin (Loon Outdoors UV Clear Fly Finish).

Polarized optical microscopy. We use a Nikon LV 100N Pol upright microscope to image patterned regions with both 20x and 50x objectives. Samples are placed on a heating stage (Instec HCS302) set to 36°C to keep 8CB in the nematic phase. Optical microscopy images are captured using a Nikon DS-Ri2 camera.

Analyzing the curvature of disclination line arcs. Videos of disclination lines are captured using bright-field microscopy and analyzed using ImageJ, TrackPy(35), and custom Python code. The contours of the disclination lines are detected using a Canny edge detection algorithm, binarized, and fit to circles using least squares fitting. For each frame i of the video, the radius of curvature $r_i \equiv 1/\kappa$ and center of the best-fit circle $\left(x_i^C, y_i^C\right)$ are determined. These circles intersect at the defect cores, corresponding to two unique points. To find the positions of these points (x,y), we minimize a cost function $\Xi = \sum_i \left(\frac{(x-x_i^c)^2+(y-y_i^c)^2)}{r_i^2} - 1\right)^2$, where the sum is over all the frames in the video. The uncertainty of each defect core's position is the cost function's value, and the distance ℓ between the defect cores is calculated using the Euclidean distance.

Jones matrix calculations. For qualitative comparison of numerical and experimental director configurations near nucleated disclination lines, we use Jones calculus to reconstruct the polarized optical microscopy (POM) texture of the director field obtained from minimization of the Landau de-Gennes free-energy. The volume of the numerically-obtained director field is discretized into volume elements (voxels) on a 3D grid, with each point at position $\boldsymbol{\rho}$ containing N voxels each of thickness Δ. It is assumed that variation in $\boldsymbol{n}$ between successive voxels is small compared to the wavelength of incident light λ, so that $\lambda \ll 1/|\nabla\hat{\mathbf{n}}|$. Each voxel ν is treated as a uniaxial birefringent optical element, represented by a 2×2 Jones matrix $\mathbb{M}_\nu$ that depends on both the extraordinary n^e and ordinary n^o indices of refraction of the LC. Light propagating through a voxel experiences an n^e dependant on the polar angle θ_ν between $\boldsymbol{n}$ and the light's propagation direction $\boldsymbol{k}_0$ given by $n^e(\theta_\nu) = n^o n^e/\sqrt{(n^o\cos\theta_\nu)^2 + (n^e\sin\theta_\nu)^2}$. We choose $\boldsymbol{k}_0 = \hat{z}$, so that the plane of polarization is the $x - z$ plane, and write the corresponding Jones matrix as,

$$\mathbb{M}_\nu(\boldsymbol{\rho}) \equiv \begin{pmatrix} e^{in_\nu^e(\theta_\nu)2\pi\frac{\Delta}{\lambda}} & 0 \\ 0 & e^{in_\nu^o 2\pi\frac{\Delta}{\lambda}} \end{pmatrix}. \qquad [13]$$

Using the 8CB's n^e and n^o at the experimental temperature and wavelength λ, we compute $\mathbb{M}_\nu(\boldsymbol{\rho})$, constructing a single operator $\gamma(\boldsymbol{\rho}) = \prod_{\nu=1}^{N}\mathbb{R}(-\phi_\nu)\mathbb{M}_\nu(\boldsymbol{\rho})\mathbb{R}(\phi_\nu)$, where $\mathbb{R}(\phi_\nu) \equiv \begin{pmatrix} \cos\phi_\nu & \sin\phi_\nu \\ -\sin\phi_\nu & \cos\phi_\nu \end{pmatrix}$ and ϕ_ν is the azimuthal component of $\hat{\mathbf{n}}$ in voxel ν. Following (36) and (37), we construct 2×2 Jones matrices for the polarizer $\mathbb{P}$ and analyzer $\mathbb{A}$. Sequential propagation of plane waves $\boldsymbol{E}_\mathbf{0}$ through $\mathbb{P}$,$\gamma(\boldsymbol{\rho})$ and $\mathbb{A}$ results in a single Jones vector $\boldsymbol{E}_T(\boldsymbol{\rho}) = \mathbb{A}\nu(\boldsymbol{\rho})\mathbb{P}\boldsymbol{E}_\mathbf{0}$. The calculated POM texture is obtained from the intensity of light transmitted through each voxel, $I_T(\boldsymbol{\rho}) = |\boldsymbol{E}_T(\boldsymbol{\rho})|^2$.

Numerical simulations. The numerical modeling of the nematic liquid crystal is achieved using the lattice-discretized Landau-de Gennes model implemented in open-Qmin(38). The configuration of a nematic liquid crystal is represented by specifying the components of the Q-tensor(38, 39) which is related to the director $\hat{\mathbf{n}}$ of a uniaxial nematic by $Q_{ij} = \frac{3}{2}S\left(n_i n_j - \frac{1}{3}\delta_{ij}\right)$, where $i,j \in \{x,y,z\}$ and S is the degree of uniaxial nematic order. To simulate a thin nematic cell, we consider a three-dimensional box of size $L \times L \times L_z$ with $L \gg L_z$. In the simulation, we use $L = 250$ and L_z between 12 and 21, expressed in units of the number of lattice sites. Note that the thickness $t = L_z - 1$, since anchoring is imposed on top and bottom layers. At every lattice point, we start with a random initial condition for Q_{ij}. We impose strong patterned planar anchoring at the top and bottom surfaces by setting the anchoring strength $W = 50$ (expressed in units of $|a|\Delta x$ where a is the Landau coefficient and Δx is the lattice spacing) for the two surfaces. This value corresponds to $W \approx 10^{-2}\mathrm{J/m^2}$ in our experimental setup. We use free boundary conditions on the side surfaces of the simulation box by setting $W = 0$. We use the Fast Inertial Relaxation Engine (FIRE) algorithm within open-Qmin(38) to minimize the total free energy until the norm of the residual force vector goes below 10^{-8} (see *SI Appendix* for details). In the energy-minimized configuration, defects are identified locally as lattice sites where the largest eigenvalue of Q falls below some threshold, typically $0.95S$.

ACKNOWLEDGMENTS. We greatly acknowledge insights, assistance, and helpful discussions with Charles Rosenblatt, David Dolgitzer and Bastián Pradenas. This research was supported by a start-up research grant from the United States-Israel Binational Science Foundation (BSF) no. 2018380 awarded to HA and FS. RLL acknowledges support from the NSF (DMR-2104747).

References.

1. JM Kosterlitz, DJ Thouless, Ordering, metastability and phase transitions in two-dimensional systems. *J. Phys. C: Solid State Phys.* **6**, 1181–1203 (1973).
2. Y Maroudas-Sacks, et al., Topological defects in the nematic order of actin fibres as organization centres of Hydra morphogenesis. *Nat. Phys.* **17**, 251–259 (2021).
3. E Brasselet, Tunable Optical Vortex Arrays from a Single Nematic Topological Defect. *Phys. Rev. Lett.* **108**, 087801 (2012).
4. C Meng, JS Wu, II Smalyukh, Topological steering of light by nematic vortices and analogy to cosmic strings. *Nat. Mater.* **22**, 64–72 (2023).
5. C Blanc, D Coursault, E Lacaze, Ordering nano- and microparticles assemblies with liquid crystals. *Liq. Cryst. Rev.* **1**, 83–109 (2013).
6. Y Luo, DA Beller, G Boniello, F Serra, KJ Stebe, Tunable colloid trajectories in nematic liquid crystals near wavy walls. *Nat. Commun.* **9**, 3841 (2018).
7. HJ Coles, MN Pivnenko, Liquid crystal 'blue phases' with a wide temperature range. *Nature* **436**, 997–1000 (2005).
8. A Sengupta, C Bahr, S Herminghaus, Topological microfluidics for flexible micro-cargo concepts. *Soft Matter* **9**, 7251 (2013).
9. JJ Sandford O'Neill, PS Salter, MJ Booth, SJ Elston, SM Morris, Electrically-tunable positioning of topological defects in liquid crystals. *Nat. Commun.* **11**, 2203 (2020).
10. BS Murray, RA Pelcovits, C Rosenblatt, Creating arbitrary arrays of two-dimensional topological defects. *Phys. Rev. E* **90**, 052501 (2014).
11. S Harkai, BS Murray, C Rosenblatt, S Kralj, Electric field driven reconfigurable multistable topological defect patterns. *Phys. Rev. Res.* **2**, 013176 (2020).
12. PM Phillips, N Mei, L Reven, A Rey, Faceted particles embedded in a nematic liquid crystal matrix: Textures, stability and filament formation. *Soft Matter* **7**, 8592–8604 (2011).
13. M Wang, Y Li, H Yokoyama, Artificial web of disclination lines in nematic liquid crystals. *Nat. Commun.* **8**, 388 (2017).
14. T Ouchi, K Imamura, K Sunami, H Yoshida, M Ozaki, Topologically Protected Generation of Stable Wall Loops in Nematic Liquid Crystals. *Phys. Rev. Lett.* **123**, 097801 (2019).
15. K Sunami, K Imamura, T Ouchi, H Yoshida, M Ozaki, Shape control of surface-stabilized disclination loops in nematic liquid crystals. *Phys. Rev. E* **97**, 020701 (2018).
16. Y Guo, et al., Photopatterned Designer Disclination Networks in Nematic Liquid Crystals (Advanced Optical Materials 16/2021). *Adv. Opt. Mater.* **9**, 2170063 (2021).
17. H Yoshida, K Asakura, J Fukuda, M Ozaki, Three-dimensional positioning and control of colloidal objects utilizing engineered liquid crystalline defect networks. *Nat. Commun.* **6**, 7180 (2015).
18. I Nys, B Berteloot, J Beeckman, K Neyts, Nematic Liquid Crystal Disclination Lines Driven by A Photoaligned Defect Grid. *Adv. Opt. Mater.* **10**, 2101626 (2022).
19. I Nys, K Chen, J Beeckman, K Neyts, Periodic Planar-Homeotropic Anchoring Realized by Photoalignment for Stabilization of Chiral Superstructures. *Adv. Opt. Mater.* **6**, 1701163 (2018).
20. B Berteloot, I Nys, G Poy, J Beeckman, K Neyts, Ring-shaped liquid crystal structures through patterned planar photo-alignment. *Soft Matter* **16**, 4999–5008 (2020).
21. J Jiang, et al., Active transformations of topological structures in light-driven nematic disclination networks. *Proc. Natl. Acad. Sci.* **119**, e2122226119 (2022).
22. PGd Gennes, J Prost, *The physics of liquid crystals*, International series of monographs on physics. (Clarendon Press, Oxford) No. 83, 2. ed., repr edition, (2013).
23. E Love, The small free vibrations and deformation of a thin elastic shell. *Philos. Transactions Royal Soc. London. (A.)* **179**, 491–546 (1888).
24. P Oswald, J Baudry, T Rondepierre, Growth below and above the spinodal limit: The cholesteric-nematic front. *Phys. Rev. E* **70**, 041702 (2004).
25. N Schopohl, TJ Sluckin, Defect core structure in nematic liquid crystals. *Phys. Rev. Lett.* **59**, 2582–2584 (1987).
26. A Shams, X Yao, JO Park, M Srinivasarao, AD Rey, Mechanisms and shape predictions of nematic disclination branching under conical confinement. *Soft Matter* **10**, 3245–3258 (2014).
27. ND Mermin, The topological theory of defects in ordered media. *Rev. Mod. Phys.* **51**, 591–648 (1979).
28. VG Chigrinov, VM Kozenkov, HS Kwok, *Photoalignment of liquid crystalline materials: physics and applications*, Wiley SID series in display technology. (Wiley, Chichester, England ; Hoboken, NJ), (2008) OCLC: ocn225429570.
29. Y Folwill, Z Zeitouny, J Lall, H Zappe, A practical guide to versatile photoalignment of azobenzenes. *Liq. Cryst.* **48**, 862–872 (2021).
30. OM Wani, P Wasylczyk, A Priimagi, Programming photoresponse in liquid crystal polymer actuators with laser projector. *Adv. Opt. Mater.* **6**, 1700949 (2017).
31. HN Padmini, M Rajabi, SV Shiyanovskii, OD Lavrentovich, Azimuthal Anchoring Strength in Photopatterned Alignment of a Nematic. *Crystals* **11**, 675 (2021).
32. C Long, et al., Frank-read mechanism in nematic liquid crystals (2022).
33. T Ishikawa, OD Lavrentovich, Crossing of disclinations in nematic slabs. *Europhys. Lett. (EPL)* **41**, 171–176 (1998).
34. J Wang, et al., Effects of humidity and surface on photoalignment of brilliant yellow. *Liq. Cryst.* **44**, 863–872 (2017).
35. D Allan, T Caswell, N Keim, C van der Wel, trackpy: Trackpy v0.3.2 (2016).
36. E Hecht, *Optics*. (Pearson Education, Inc, Boston), 5 ed edition, (2017).
37. PW Ellis, E Pairam, A Fernández-Nieves, Simulating optical polarizing microscopy textures using Jones calculus: a review exemplified with nematic liquid crystal tori. *J. Phys. D: Appl. Phys.* **52**, 213001 (2019).
38. DM Sussman, DA Beller, Fast, scalable, and interactive software for landau-de gennes numerical modeling of nematic topological defects. *Front. Phys.* **7**, 204 (2019).
39. NJ Mottram, CJP Newton, Introduction to Q-tensor theory. *arXiv:1409.3542* (2014).